

Neural density functionals: Local learning and pair-correlation matching

Florian Sammüller¹ and Matthias Schmidt¹

¹*Theoretische Physik II, Physikalisches Institut, Universität Bayreuth, D-95447 Bayreuth, Germany**
(Dated: 5 June 2024)

Recently Dijkman *et al.* (arxiv:2403.15007) proposed training classical neural density functionals via bulk pair-correlation matching. We show their method to be an efficient regularizer for neural functionals based on local learning of inhomogeneous one-body direct correlations [Sammüller *et al.*, Proc. Natl. Acad. Sci. **120**, e2312484120 (2023)]. We demonstrate that local one-body learning allows flexible neural modelling of the full Mermin-Evans density functional map, but that bulk pair-correlation matching alone does not. Using spatial localization gives access to accurate neural free energy functionals, including convolutional neural networks, that transcend the training box.

As machine learning and density functional theory [1–4] share high computational efficiency, it is natural to use neural networks to construct workable and accurate approximations for the required density functional relationships in the classical [5–16] and quantum realms [17–24]. This common goal to make progress is nevertheless approached from quite different directions and a considerable range of different machine learning strategies have been put forward [5–24]. The task is both important and challenging. Overcoming the limited availability of flexible classical density functional approximations would open up the study of a much broader class of soft matter systems than is currently accessible via, e.g., the hard sphere perturbation paradigm of fundamental-measure theory [25–27] combined with mean-field attraction, as used in recent work [28–30].

In the classical context, typically the excess free energy functional $F_{\text{exc}}[\rho]$ is the object chosen to be approximated [1, 2]. We recall that $F_{\text{exc}}[\rho]$ is the nontrivial contribution to the total grand potential functional $\Omega[\rho] = F_{\text{id}}[\rho] + F_{\text{exc}}[\rho] + \int d\mathbf{r} \rho(\mathbf{r})[V_{\text{ext}}(\mathbf{r}) - \mu]$, where the ideal gas free energy functional $F_{\text{id}}[\rho]$ is known explicitly, $V_{\text{ext}}(\mathbf{r})$ is the external potential that generates spatial inhomogeneity and μ is the chemical potential that together with absolute temperature T determines the thermodynamic conditions. The Mermin-Evans variational principle [1, 31] ascertains that $\Omega[\rho]$ is minimized by the true equilibrium density profile $\rho(\mathbf{r})$, as a function of position \mathbf{r} across the system, and that the minimum gives the equilibrium value of the grand potential.

The effects of the interparticle interactions are contained in $F_{\text{exc}}[\rho]$, which per se is not easily accessible and requires the development of careful modelling strategies. Neural networks suit this task very well, due to the clearcut correspondence between the spatially resolved input density profile $\rho(\mathbf{r})$ and the excess free energy $F_{\text{exc}}[\rho]$ as a global output value. Reference data for supervised machine learning is provided by many-body simulations [32–34], which hence offers the perspective of making theoretical predictions with simulation precision.

Two very recent implementations use neural networks to represent the functional relationship of either the

global excess free energy $F_{\text{exc}}[\rho]$ [10] or the closely related one-body direct correlation functional $c_1(\mathbf{r}; [\rho])$ [12, 13]. The training strategy in Ref. [10] employs bulk pair-correlation matching, while Refs. [12, 13] utilize a local learning approach involving inhomogeneous one-body profiles. A major appeal of the former [10] is the sole requirement of simulation input in the form of bulk radial distribution functions $g(r)$ at different densities for the particular model under investigation. Local learning [12, 13] rather requires inhomogeneous density profiles as training data. Going beyond mere interpolation tasks, the resulting neural functionals [12, 13] were shown to be fit for carrying out deep functional calculus based on exact sum rules and on functional identities. Both methods were argued to be numerically highly accurate [10, 12, 13].

In this Letter we contrast and cross-fertilize the underlying concepts of pair-correlation matching [10] and of inhomogeneous one-body learning [12, 13]. We show how to incorporate pair-correlation matching in a local learning strategy, which then retains the ability of transcending beyond the box size of the training simulations. In keeping with statistical mechanics, pair-correlation matching constitutes a physics-based regularizer for the training loss, thereby avoiding potential problems of more generic regularization methods [35]. We also demonstrate based on comparison to reference simulation data and on violation of internal sum rule consistency, that training density-functional dependence solely with bulk densities can yield unreliable neural performance in general inhomogeneous situations. We show that the local learning concept generalizes beyond constructing neural one-body direct correlations, laying out two explicit strategies that make $F_{\text{exc}}[\rho]$ directly accessible.

We first describe key ideas of pair-correlation matching as proposed by Dijkman *et al.* [10] to construct a neural network that represents the functional $F_{\text{exc}}[\rho]$. Their method exploits that $F_{\text{exc}}[\rho]$ is a generating functional for the hierarchy of direct correlation functionals. Specifically, at second order the two-body direct correlation

functional is obtained [1, 2]:

$$c_2(\mathbf{r}, \mathbf{r}'; [\rho]) = -\frac{\delta^2 \beta F_{\text{exc}}[\rho]}{\delta \rho(\mathbf{r}) \delta \rho(\mathbf{r}')}, \quad (1)$$

where $\delta/\delta \rho(\mathbf{r})$ indicates the functional derivative with respect to $\rho(\mathbf{r})$ and $\beta = 1/(k_B T)$ with Boltzmann constant k_B . When specializing to the important, yet restricted, case of bulk fluids, the density profile is constant, $\rho(\mathbf{r}) = \rho_b = \text{const}$, and the bulk pair direct correlation function $c_2(r; \rho_b)$ of liquid state theory is recovered [2]. This constitutes a functional reduction

$$c_2(r; \rho_b) = c_2(\mathbf{r}, \mathbf{r}'; [\rho = \rho_b]), \quad (2)$$

where the spatial dependence on \mathbf{r} and \mathbf{r}' simplifies to the dependence on radial distance $r = |\mathbf{r} - \mathbf{r}'|$ on the left hand side. Also the general functional dependence on the entirety of the density profile $\rho(\mathbf{r})$ in Eq. (1) is reduced to a mere parametric dependence on the value of the bulk density ρ_b in Eq. (2).

Pair-correlation matching [10] exploits that results for pair correlation (or radial distribution) functions $g(r)$ are readily accessible via simulations. Using the total correlation function $h(r) = g(r) - 1$, the bulk Ornstein-Zernike equation ascertains that $h(r) = c_2^{\text{ref}}(r) + \rho_b c_2^{\text{ref}}(r) \star h(r)$, where the star indicates spatial convolution. We have denoted the bulk two-body direct correlation function from this route by $c_2^{\text{ref}}(r)$, as originating from the simulation data for $g(r)$. Numerical solution of the Ornstein-Zernike equation yields quasi-exact reference results for $c_2^{\text{ref}}(r)$; details are given in the SI [36]. Pair-correlation matching [10] trains $F_{\text{exc}}[\rho]$ as a convolutional neural network by minimizing the difference of $c_2(r; \rho_b)$, as obtained via Eq. (1) and functional reduction (2), against the quasi-exact reference data for $c_2^{\text{ref}}(r)$ from simulations and Ornstein-Zernike inversion. Thereby the functional derivative in Eq. (1) is performed via automatic differentiation (autodiff) [10, 12–14, 37]. The aim is to achieve equality,

$$c_2(r; \rho_b) = c_2^{\text{ref}}(r; \rho_b). \quad (3)$$

Crucially, during training the neural functional is only evaluated via its Hessian with respect to the input in Eq. (2) at constant density profiles $\rho(\mathbf{r}) = \rho_b$ with varying values of ρ_b . No inhomogeneous density profiles are encountered during training.

By contrast local direct correlation learning [12, 13] starts with the standard liquid state relationship

$$c_1^{\text{ref}}(\mathbf{r}) = \ln \rho(\mathbf{r}) + \beta V_{\text{ext}}(\mathbf{r}) - \beta \mu, \quad (4)$$

where $c_1^{\text{ref}}(\mathbf{r})$ is the one-body direct correlation function that forms the reference. One exploits that all quantities on the right hand side of Eq. (4) are either known $[\beta, \mu, V_{\text{ext}}(\mathbf{r})]$ or are directly accessible in simulations $[\rho(\mathbf{r})]$; potentially via force sampling [38]. Hence

one can construct data for $c_1^{\text{ref}}(\mathbf{r})$ to act as a reference. The one-body direct correlation function is then transcended to a density functional, recall: $c_1(\mathbf{r}; [\rho]) = -\delta \beta F_{\text{exc}}[\rho] / \delta \rho(\mathbf{r})$. The direct correlation learning [12, 13] represents $c_1(\mathbf{r}; [\rho])$ at a considered position \mathbf{r} directly as a neural network, with a simple yet very general multi-layer perceptron architecture. Supervised training is used to approach

$$c_1(\mathbf{r}; [\rho]) = c_1^{\text{ref}}(\mathbf{r}; [\rho]), \quad (5)$$

where the left hand side is the output of the neural functional and the right hand side is the reference obtained via Eq. (4) with simulation input for $\rho(\mathbf{r})$. Training to optimize the matching condition (5) is performed across a range of (several hundred) training systems and hence differing shapes of the density profile $\rho(\mathbf{r})$. The resulting functional can then be applied independently of the system size of the original simulations, thus enabling to make predictions “beyond-the-box” [12, 13].

Using autodiff to functionally differentiate the one-body direct correlation functional $c_1(\mathbf{r}; [\rho])$ yields the two-body direct correlation functional

$$c_2(\mathbf{r}, \mathbf{r}'; [\rho]) = \frac{\delta c_1(\mathbf{r}; [\rho])}{\delta \rho(\mathbf{r}')}, \quad (6)$$

which is now expressed as a first derivative rather than (and formally consistent with) the second functional derivative in Eq. (1). This implies a significant reduction in terms of computational complexity for the case of short-ranged (truncated) interparticle interactions. Performing the functional reduction (2) then gives results for $c_2(r; \rho_b)$ with genuine predictive status as no information about $c_2^{\text{ref}}(r; \rho_b)$ has entered the local learning scheme. Hence the bulk direct correlation matching (3) can be used as an *a posteriori* quality check of the neural functional $c_1(\mathbf{r}; [\rho])$. Similarly, the exchange symmetry $c_2(\mathbf{r}, \mathbf{r}'; [\rho]) = c_2(\mathbf{r}', \mathbf{r}; [\rho])$, which follows from interchanging the order of derivatives in Eq. (1), is a non-trivial consistency test.

We have kept the presentation general, but inline with Refs. [10–13] we train all neural functionals in planar geometry. We use the supercritical Lennard-Jones fluid at reduced temperature $k_B T / \epsilon = 1.5$ as a generic model system. Planar geometry offers computational benefits and it constitutes arguably the most important type of inhomogeneity due to a multitude of relevant interfacial and substrate applications (including phase transitions). The technical details of the conversion from radial to planar geometry are described in our SI [36] and all data is openly available [39].

To combine the virtues of the different approaches, we first incorporate the pair-correlation matching (3) into the local learning method by using Eq. (6) to express $c_2(\mathbf{r}, \mathbf{r}'; [\rho])$ and then proceed to the functional reduction (2). The loss that is optimized in the supervised

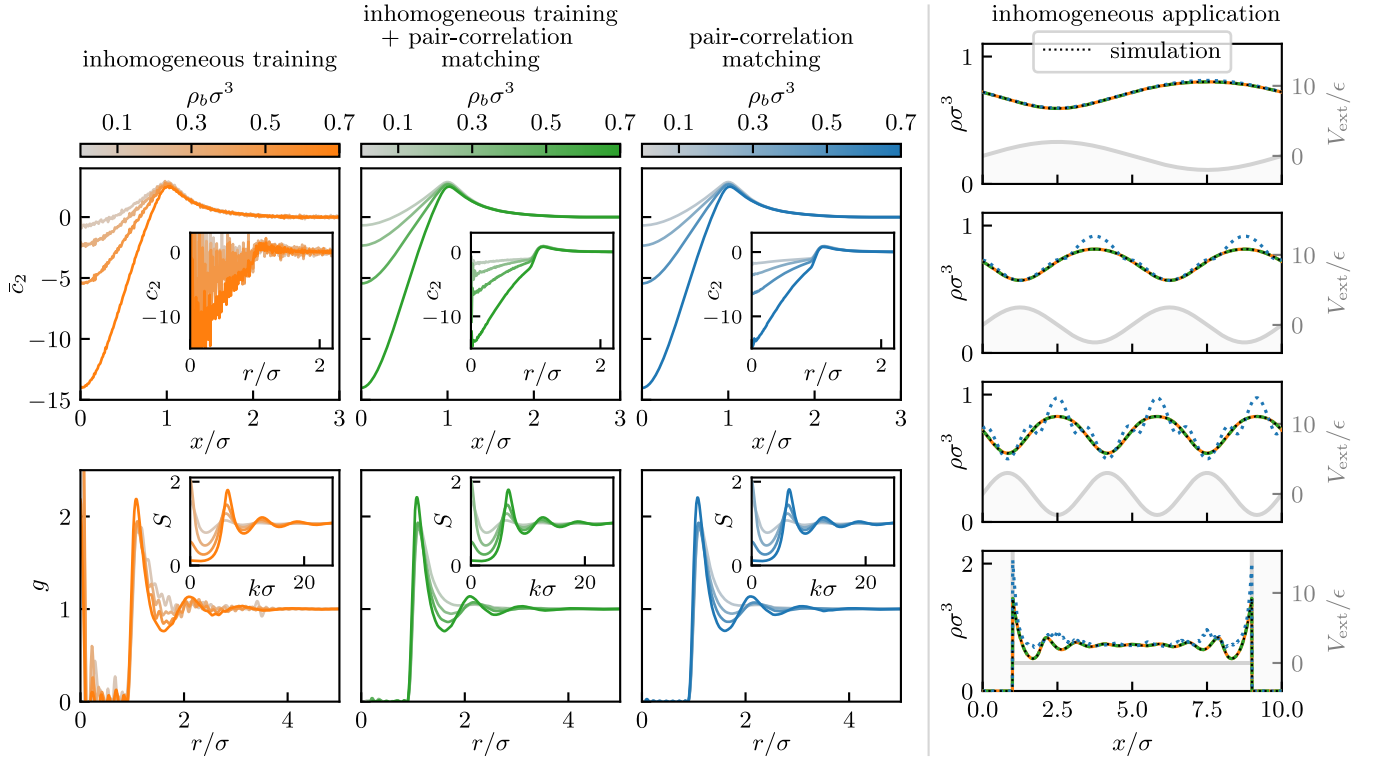


FIG. 1. Neural functional results for bulk pair structure and planar inhomogeneous density profiles. We show bulk results from neural functionals obtained via one-body inhomogeneous training (first column), adding the bulk pair correlation regularization (second column), and from pure pair-correlation matching (third column). The supercritical Lennard-Jones fluid is at reduced temperature $k_B T/\epsilon = 1.5$ and different scaled bulk densities $\rho_b \sigma^3$ (color bar). Shown is the bulk pair direct correlation function $\bar{c}_2(x; \rho_b)$ in planar geometry as a function of scaled planar distance x/σ obtained via autodiff (6) (top panels) and $c_2(r; \rho_b)$ as a function of radial distance r/σ (insets in top panels). The Ornstein-Zernike relation yields the corresponding pair correlation function $g(r)$ (bottom panels) and bulk structure factor $S(k)$ (insets in bottom panels). Also shown are predictions from the same three neural functionals for planar inhomogeneities (fourth column) as induced by an external potential $V_{\text{ext}}(x)$ (gray lines) at $\mu/\epsilon = 0$. Results from the pure pair-correlation matched functional deviate increasingly from those with inhomogeneous training, which remain almost identical to the simulation reference (thin dotted lines) upon increasing inhomogeneity (from top to bottom) even for confinement between parallel hard walls (bottom panel).

machine learning remains based on the one-body direct correlation matching (5) but it is supplemented by a regularizer based on Eq. (3). We find that using the regularizer improves the training dynamics and the overall quality of the results achieved, as is desired and expected when supplying additional information about bulk correlations; details are given in the SI [36]. Note the inhomogeneous training data is re-used from Ref. [12]. As a test, we display results for the predicted bulk structure from both un-regularized one-body learning and pair matching-regularized one-body learning in Fig. 1. The results with regularization are smoother and the predicted radial distribution functions $g(r)$ are closer to zero inside the core, consistent with the expectation based on the supply of bulk information into the scheme.

We have also trained a one-body correlation functional based on pair-correlation matching alone with no information about inhomogeneous systems entering. This is potentially important as it would remove the need to

generate inhomogeneous training data, as is argued in Ref. [10]. Within our scheme the method is straightforward to implement by basing the loss solely on the bulk direct correlation matching (3). Similar to Ref. [10] we provide the required integration constants by noting from Eq. (4) that $\beta \mu_{\text{exc}} \equiv \beta \mu - \ln \rho_b = -c_1(\mathbf{r}; [\rho])$, which the neural functional delivers with constant density input, $\rho(\mathbf{r}) = \rho_b$. Results for the excess chemical potential μ_{exc} are obtained from simulating bulk systems with $V_{\text{ext}}(\mathbf{r}) = 0$. We find despite apparently successful performance in training metrics that the pair-correlation matched neural functional $c_1(\mathbf{r}; [\rho])$ is of significantly poorer quality than those from the two local one-body learning methods, which rely on inhomogeneous training data. This becomes clear in predictions for inhomogeneous systems, where the results of the former neural functional fall short of those from the inhomogeneously trained networks, as shown in Fig. 1, Col. 4. Also the exchange symmetry $c_2(\mathbf{r}, \mathbf{r}'; [\rho]) = c_2(\mathbf{r}', \mathbf{r}; [\rho])$, which is

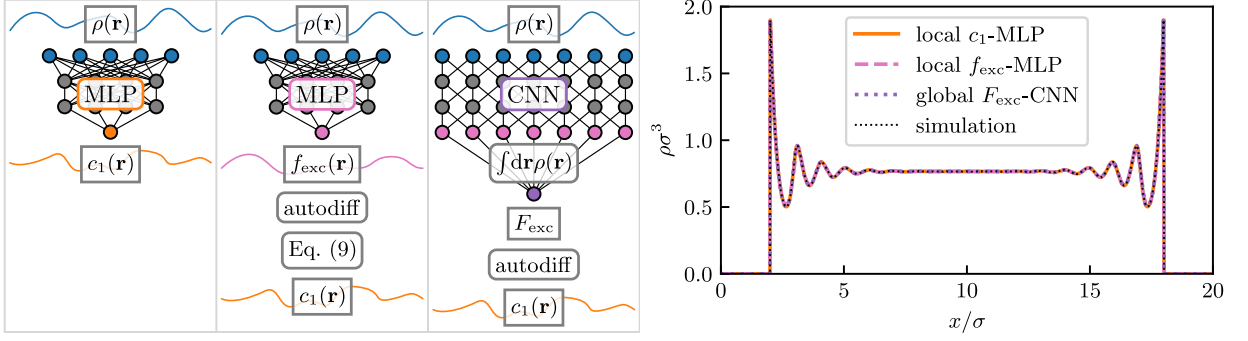


FIG. 2. Illustration of the three different network architectures for neural functionals. Shown are the multilayer perceptrons (MLP) for local learning of $c_1(\mathbf{r}; [\rho])$ (first column) and for $f_{\text{exc}}(\mathbf{r}; [\rho])$ (second column), and the convolutional neural network (CNN) for $F_{\text{exc}}[\rho]$. Corresponding predictions for the scaled density profiles $\rho(x)\sigma^3$ (fourth column) are for the supercritical Lennard-Jones fluid with $\mu/\epsilon = 1$ and $k_B T/\epsilon = 1.5$ confined between two hard walls at $x/\sigma = 2$ and $x/\sigma = 18$. Results for $\rho(x)$ are shown from density functional minimization using $c_1(x; [\rho])$ obtained from local learning according to Eq. (5), from local learning of $f_{\text{exc}}(x; [\rho])$ via Eq. (9), and from inhomogeneous one-body training of the convolutional neural network representation of $F_{\text{exc}}[\rho]$. The predictions from the three different neural functionals are identical to the simulation reference (thin dotted line) on the scale of the plot.

a necessary Cauchy-Riemann-like integrability condition for the existence of a generating functional $F_{\text{exc}}[\rho]$ according to Eq. (1), is violated, as shown in the SI [36]. The method of Ref. [10] satisfies the exchange symmetry by construction via the neural representation of $F_{\text{exc}}[\rho]$ and the interchangeability of the order of the two derivatives in Eq. (1).

We next describe two variants of inhomogeneous one-body learning for modelling directly the generating functional $F_{\text{exc}}[\rho]$. We work with a localized excess free energy integrand $f_{\text{exc}}(\mathbf{r}; [\rho])$ such that

$$F_{\text{exc}}[\rho] = \int d\mathbf{r} \rho(\mathbf{r}) f_{\text{exc}}(\mathbf{r}; [\rho]), \quad (7)$$

where the spatial integration domain is the entire system volume. The general functional integral $\beta F_{\text{exc}}[\rho] = -\int \mathcal{D}[\rho] c_1(\mathbf{r}; [\rho])$ is parameterized by Eq. (7) when choosing [3, 13]

$$-\beta f_{\text{exc}}(\mathbf{r}; [\rho]) = \int_0^1 da c_1(\mathbf{r}; [a\rho]). \quad (8)$$

where $a\rho(\mathbf{r})$ is a scaled version of the density profile. The integrals in Eqs. (7) and (8) can be performed numerically with high efficiency to obtain the value of the excess free energy [12, 13].

We obtain the corresponding one-body direct correlation functional by recalling $c_1(\mathbf{r}; [\rho]) = -\delta\beta F_{\text{exc}}[\rho]/\delta\rho(\mathbf{r})$ and inserting $F_{\text{exc}}[\rho]$ in the form (7), which gives

$$c_1(\mathbf{r}; [\rho]) = -\beta f_{\text{exc}}(\mathbf{r}; [\rho]) - \int d\mathbf{r}' \rho(\mathbf{r}') \frac{\delta\beta f_{\text{exc}}(\mathbf{r}; [\rho])}{\delta\rho(\mathbf{r}')} \quad (9)$$

We have exchanged \mathbf{r} and \mathbf{r}' according to the symmetry $\delta f_{\text{exc}}(\mathbf{r}'; [\rho])/\delta\rho(\mathbf{r}) = \delta f_{\text{exc}}(\mathbf{r}; [\rho])/\delta\rho(\mathbf{r}')$; this iden-

tity follows from differentiating Eq. (8) and from the exchange symmetry of $c_2(\mathbf{r}, \mathbf{r}'; [\rho])$. The form (9) is suitable for the application to local learning.

In our first free energy method we represent $f_{\text{exc}}(\mathbf{r}; [\rho])$ as a neural functional and perform one-body direct correlation matching via Eq. (5) on the basis of Eq. (9), where autodiff is used to carry out the functional derivative. The second free energy method uses a convolutional neural network architecture similar to that of Ref. [10] to implement via $f_{\text{exc}}(\mathbf{r}; [\rho])$ the excess free energy functional $F_{\text{exc}}[\rho]$ in the structure of Eq. (7). We thereby perform no pooling (coarse-graining, as is common practice [35]) and design a final layer that represents $f_{\text{exc}}(\mathbf{r}; [\rho])$ which is then multiplied by $\rho(\mathbf{r})$ and integrated according to Eq. (7) for the global value of $F_{\text{exc}}[\rho]$; details are given in the SI [36]. This specific convolutional neural network design extends naturally to arbitrary system sizes, thus replicating the capability of the local correlation learning for making predictions “beyond-the-box” [12, 13]. Illustrations of the different neural functionals together with representative results from the three methods for planar density profiles $\rho(x)$ of a Lennard-Jones fluid confined between parallel hard walls are shown Fig. 2. Having been trained with the same inhomogeneous one-body profiles from grand canonical Monte Carlo simulations [12], all methods give an excellent account of the highly inhomogeneous spatial fluid structure.

We conclude with several conceptual points related to the inherent functional reduction (2) of bulk pair-correlation matching [10]. The feeding of knowledge of $g(r)$ into the neural functional constitutes a very significant amount of information about the system under consideration. Henderson’s uniqueness theorem [40] formally ensures that for systems interacting solely with a pair potential $\phi(r)$, perfect knowledge of $g(r)$, at a sin-

gle statepoint, is sufficient to determine $\phi(r)$. Density functional theory [1] then implies that $F_{\text{exc}}[\rho]$ is uniquely determined in principle, given the information that no higher-body interparticle interactions are present [41].

However, it is difficult to see why a neural functional trained through the aperture of the functional reduction (2) would render Henderson’s theorem operational. As the density functional framework (1)–(3), utilized within the pair-correlation matching, applies equally to a system with many-body interparticle interactions, we see no mechanism in Ref. [10] that would intrinsically reduce $F_{\text{exc}}[\rho]$ to pair interactions only (see Ref. [41] for a related discussion in the context of simulation work). This situation cannot be remedied by supplying $g(r)$ in more abundance and with higher precision. In contrast the one-body matching condition (5) allows for full exploration of the entire density functional dependence for any given form of the underlying Hamiltonian, which gives a formal mechanism to rationalize the high quality of our correspondingly obtained results.

In future work it would be interesting to utilize test particle concepts [42] to identify $\rho(\mathbf{r}) = \rho_b g(r)$ upon setting $V_{\text{ext}}(\mathbf{r}) = \phi(r)$, as also explored dynamically [43–45] and quantum mechanically [46]. The use of the force density integral $\rho(\mathbf{r})\nabla c_1(\mathbf{r};[\rho]) = -\int d\mathbf{r}'\rho_2(\mathbf{r},\mathbf{r}')\nabla\beta\phi(|\mathbf{r}-\mathbf{r}'|)$ [1, 2, 47, 48] could be beneficial for making progress despite an increase in complexity [49, 50]. Localized forces are also relevant for functional treatments of general observables [14] and for nonequilibrium flow [11, 15].

We thank Jacobus Dijkman, Max Welling, Jan-Willem van de Meent, Bernd Ensing, Kieron Burke, Marjolein Dijkstra, Bob Evans, and Stefanie Kampa for useful discussions.

* Florian.Sammueler@uni-bayreuth.de

- [1] R. Evans, The nature of the liquid-vapour interface and other topics in the statistical mechanics of non-uniform, classical fluids, *Adv. Phys.* **28**, 143 (1979).
- [2] J. P. Hansen and I. R. McDonald, *Theory of Simple Liquids*, 4th ed. (Academic Press, London, 2013).
- [3] R. Evans, Density functionals in the theory of nonuniform fluids, Chap. 3 in *Fundamentals of Inhomogeneous Fluids*, edited by D. Henderson (Dekker, New York, 1992).
- [4] R. Evans, M. Oettel, R. Roth, and G. Kahl, New developments in classical density functional theory, *J. Phys.: Condens. Matter* **28**, 240401 (2016).
- [5] S.-C. Lin and M. Oettel, A classical density functional from machine learning and a convolutional neural network, *SciPost Phys.* **6**, 025 (2019).
- [6] S.-C. Lin, G. Martius, and M. Oettel, Analytical classical density functionals from an equation learning network, *J. Chem. Phys.* **152**, 021102 (2020).
- [7] P. Cats, S. Kuipers, S. de Wind, R. van Damme, G. M. Coli, M. Dijkstra, and R. van Roij, Machine-learning free-energy functionals using density profiles from simulations, *APL Mater.* **9**, 031109 (2021).
- [8] P. Yatsyshin, S. Kalliadasis, and A. B. Duncan, Physics-constrained Bayesian inference of state functions in classical density-functional theory, *J. Chem. Phys.* **156**, 074105 (2022).
- [9] A. Malpica-Morales, P. Yatsyshin, M. A. Duran-Olivencia, and S. Kalliadasis, Physics-informed Bayesian inference of external potentials in classical density functional theory, *J. Chem. Phys.* **159**, 104109 (2023).
- [10] J. Dijkman, M. Dijkstra, R. van Roij, M. Welling, J.-W. van de Meent, and B. Ensing, Learning Neural Free-Energy Functionals with Pair-Correlation Matching arxiv:2403.15007.
- [11] D. de las Heras, T. Zimmermann, F. Sammüller, S. Hermann, and M. Schmidt, Perspective: How to overcome dynamical density functional theory, *J. Phys.: Condens. Matter* **35**, 271501 (2023). (Invited Perspective).
- [12] F. Sammüller, S. Hermann, D. de las Heras, and M. Schmidt, Neural functional theory for inhomogeneous fluids: Fundamentals and applications, *Proc. Natl. Acad. Sci.* **120**, e2312484120 (2023).
- [13] F. Sammüller, S. Hermann, and M. Schmidt, Why neural functionals suit statistical mechanics, *J. Phys.: Condens. Matter* **36**, 243002 (2024) (Invited Topical Review).
- [14] F. Sammüller, S. Robitschko, S. Hermann, and M. Schmidt, Hyper-density functional theory of soft matter *Phys. Rev. Lett.* (submitted), arxiv:2403.07845.
- [15] T. Zimmermann, F. Sammüller, S. Hermann, M. Schmidt, and D. de las Heras, Neural force functional for non-equilibrium many-body colloidal systems (to be published).
- [16] A. Simon, J. Weimar, G. Martius, and M. Oettel, Machine learning of a density functional for anisotropic patchy particles, *J. Chem. Theory Comput.* **20**, 1062 (2024).
- [17] R. Nagai, R. Akashi, S. Sasaki, and S. Tsuneyuki, Neural-network Kohn-Sham exchange-correlation potential and its out-of-training transferability, *J. Chem. Phys.* **148**, 241737 (2018).
- [18] J. Schmidt, C. L. Benavides-Riveros, and M. A. L. Marques, Machine learning the physical nonlocal exchange-correlation functional of density-functional theory, *J. Phys. Chem. Lett.* **10**, 6425 (2019).
- [19] Y. Zhou, J. Wu, S. Chen, and G. Chen, Toward the exact exchange-correlation potential: A three-dimensional convolutional neural network construct, *J. Phys. Chem. Lett.* **10**, 7264 (2019).
- [20] R. Nagai, R. Akashi, and O. Sugino, Completing density functional theory by machine learning hidden messages from molecules, *npj Comput. Mater.* **6**, 43 (2020).
- [21] L. Li, S. Hoyer, R. Pederson, R. Sun, E. D. Cubuk, P. Riley, and K. Burke, Kohn-Sham equations as regularizer: Building prior knowledge into machine-learned physics, *Phys. Rev. Lett.* **126**, 036401 (2021).
- [22] H. Li, N. Zou, M. Ye, R. Xu, X. Gong, and W. Duan, Deep-learning density functional theory Hamiltonian for efficient ab initio electronic-structure calculation, *Nat. Comput. Sci.* **2**, 367 (2022).
- [23] R. Pederson, B. Kalita, and K. Burke, Machine learning and density functional theory, *Nat. Rev. Phys.* **4**, 357 (2022).
- [24] J. Gedeon, J. Schmidt, M. J. P. Hodgson, J. Wetherell, C. L. Benavides-Riveros, and M. A. L. Marques, Machine

- learning the derivative discontinuity of density-functional theory, *Mach. Learn.: Sci. Technol.* **3**, 015011 (2022).
- [25] Y. Rosenfeld, Free-energy model for the inhomogeneous hard-sphere fluid mixture and density-functional theory of freezing, *Phys. Rev. Lett.* **63**, 980 (1989).
 - [26] H. Hansen-Goos and R. Roth, Density functional theory for hard-sphere mixtures: the White Bear version mark II, *J. Phys.: Condens. Matter* **18**, 8413 (2006).
 - [27] R. Roth, Fundamental measure theory for hard-sphere mixtures: a review, *J. Phys.: Condens. Matter* **22**, 063102 (2010).
 - [28] R. Evans, M. C. Stewart, and N. B. Wilding, A unified description of hydrophilic and superhydrophobic surfaces in terms of the wetting and drying transitions of liquids, *Proc. Natl. Acad. Sci.* **116**, 23901 (2019).
 - [29] M. K. Coe, R. Evans, and N. B. Wilding, Density depletion and enhanced fluctuations in water near hydrophobic solutes: identifying the underlying physics, *Phys. Rev. Lett.* **128**, 045501 (2022).
 - [30] M. K. Coe, R. Evans, and N. B. Wilding, Understanding the physics of hydrophobic solvation, *J. Chem. Phys.* **158**, 034508 (2023).
 - [31] N. D. Mermin, Thermal properties of the inhomogeneous electron gas, *Phys. Rev.* **137**, A1441 (1965).
 - [32] D. Frenkel and B. Smit, *Understanding Molecular Simulation: From Algorithms to Applications*, 3rd ed. (Academic Press, London, 2023).
 - [33] N. B. Wilding, Computer simulation of fluid phase transitions, *Am. J. Phys.* **69**, 1147 (2001).
 - [34] A. V. Brukhno, J. Grant, T. L. Underwood, K. Stratford, S. C. Parker, J. A. Purton, and N. B. Wilding, DL_MONTE: a multipurpose code for Monte Carlo simulation, *Molec. Simul.* **47**, 131 (2021).
 - [35] F. Chollet, *Deep Learning with Python* (Manning Publications, 2017).
 - [36] F. Sammüller and M. Schmidt, Supplementary Information.
 - [37] A. G. Baydin, B. A. Pearlmutter, A. A. Radul, and J. M. Siskind, Automatic differentiation in machine learning: A survey, *J. Machine Learning Res.* **18**, 1 (2018).
 - [38] B. Rotenberg, Use the force! Reduced variance estimators for densities, radial distribution functions, and local mobilities in molecular simulations, *J. Chem. Phys.* **153**, 150902 (2020).
 - [39] Code, simulation data, and neural functionals are available at: <https://github.com/sfalmo/local-pair-matching>.
 - [40] R. L. Henderson, A uniqueness theorem for fluid pair correlation functions, *Phys. Lett. A* **49**, 197 (1974).
 - [41] R. Evans, Comment on reverse Monte Carlo simulation, *Molec. Sim.* **4**, 409 (1990).
 - [42] J. K. Percus, Approximation methods in classical statistical mechanics, *Phys. Rev. Lett.* **8**, 462 (1962).
 - [43] L. L. Treffenstädt and M. Schmidt, Universality in driven and equilibrium hard sphere liquid dynamics, *Phys. Rev. Lett.* **126**, 058002 (2021).
 - [44] L. L. Treffenstädt, T. Schindler, M. Schmidt, Dynamic decay and superadiabatic forces in the van Hove dynamics of bulk hard sphere fluids, *SciPost Phys.* **12**, 133 (2022).
 - [45] M. Schmidt, Power functional theory for many-body dynamics, *Rev. Mod. Phys.* **94**, 015007 (2022).
 - [46] R. J. McCarty, D. Perchak, R. Pederson, R. Evans, Y. Qiu, S. R. White, and K. Burke, Bypassing the energy functional in density functional theory: direct calculation of electronic energies from conditional probability densities, *Phys. Rev. Lett.* **125**, 266401 (2020).
 - [47] J. Yvon, La théorie statistique des fluides et l'équation d'état (in French), *Actualités Scientifiques et Industrielles*, (Hermann & Cie., Paris, 1935).
 - [48] M. Born and H. S. Green, A general kinetic theory of liquids I. The molecular distribution functions, *Proc. R. Soc. London, Ser. A* **188**, 10 (1946).
 - [49] S. M. Tschopp, F. Sammüller, S. Hermann, M. Schmidt, and J. M. Brader, Force density functional theory in- and out-of-equilibrium, *Phys. Rev. E* **106**, 014115 (2022).
 - [50] F. Sammüller, S. Hermann, and M. Schmidt, Comparative study of force-based classical density functional theory, *Phys. Rev. E* **107**, 034109 (2023).

Supplementary Information for “Neural density functionals: Local learning and pair-correlation matching”

Florian Sammüller and Matthias Schmidt

*Theoretische Physik II, Physikalisches Institut, Universität Bayreuth, D-95447 Bayreuth, Germany**

(Dated: June 5, 2024)

I. LOCAL INHOMOGENEOUS ONE-BODY LEARNING

A. Training data

Training of the neural correlation functional proceeds as in Ref. [1] with GCMC simulation data for inhomogeneous randomized external potentials. We consider the truncated ($r_c = 2.5\sigma$) Lennard-Jones fluid at constant supercritical [2] temperature $k_B T/\epsilon = 1.5$. We reuse the training data set of Ref. [1] consisting of 500 simulation results in a box of length 20σ in the inhomogeneous x -direction and lateral lengths of 10σ . The inhomogeneities in the considered training set are substantial and result in local density maxima of up to $\rho(x)\sigma^3 \lesssim 6$, which nevertheless poses no difficulty during sampling (in contrast to accessing the radial distribution function $g(r)$ for large bulk densities, cf. Sec. III A). The data set is deposited in Zenodo [3].

One-body direct correlation profiles are calculated pointwise from the sampled density profiles $\rho(x)$ according to

$$c_1^{\text{ref}}(x; [\rho]) = \ln \rho(x) + \beta V_{\text{ext}}(x) - \beta \mu, \quad (1)$$

where the external potential $V_{\text{ext}}(x)$, chemical potential μ and inverse temperature $\beta = 1/(k_B T)$ are known input quantities of the simulations. The logarithm in Eq. (1) is understood as $\ln(\rho(x)\Lambda^3)$, where the thermal wavelength Λ is set to the particle size σ , which defines our unit of length.

B. Neural network and training procedure

The neural network used for the local representation of the one-body direct correlation functional $c_1(x; [\rho])$ possesses a straightforward multilayer perceptron (MLP) architecture, see Fig. S5. We use three hidden layers with 512 nodes and smooth non-linear activation functions (Gaussian error linear units, “GELU”). The input layer consists of 701 nodes, as the density profile is provided in a window of size 3.5σ around the location of interest with a discretization interval of $\Delta x = 0.01\sigma$.

Training the neural network on the basis of inhomogeneous one-body learning amounts to minimizing the loss

$$L_{\text{inhom}} = \sum_{i,j} (c_1(x_i; [\rho_j]) - c_1^{\text{ref}}(x_i; [\rho_j]))^2, \quad (2)$$

where the neural network prediction $c_1(x_i; [\rho_j])$ is compared to the reference data $c_1^{\text{ref}}(x_i; [\rho_j])$ for each discretized location x_i of every inhomogeneous system j in the training set. Code, simulation data and trained models are openly available [4].

C. Applications

For the prediction of density profiles, rearranging Eq. (1) yields

$$\rho(x) = \exp(-\beta(V_{\text{ext}}(x) - \mu) + c_1(x; [\rho])), \quad (3)$$

which constitutes the standard Euler-Lagrange equation of DFT. Given an analytical or neural representation of $c_1(x; [\rho])$, Eq. (3) can be solved self-consistently for $\rho(x)$ with a standard Picard iteration [1].

Accessing structural information on the pair-correlation level is facilitated by functional differentiation of $c_1(x; [\rho])$, which yields the two-body direct correlation functional

$$c_2(x, x'; [\rho]) = \frac{\delta c_1(x; [\rho])}{\delta \rho(x')}. \quad (4)$$

The functional derivative can be evaluated efficiently for general density input $\rho(x)$ by automatic differentiation and normalization with the discretization interval Δx . Using automatic differentiation is particularly suitable and natural in case of a neural-network-based representation of $c_1(x; [\rho])$.

II. BULK PAIR-CORRELATIONS

The considered neural functionals operate on the level of direct correlations in planar geometry. In the following, we lay out conversions between radial and planar geometry in direct and Fourier space. The Ornstein-Zernike equation is utilized to obtain total correlation functions from neural predictions and, inversely, to convert radial distribution functions $g(r)$ from direct measurement in simulation to corresponding direct correlation functions for use in the pair-correlation matching, see Sec. III A.

* Florian.Sammueler@uni-bayreuth.de

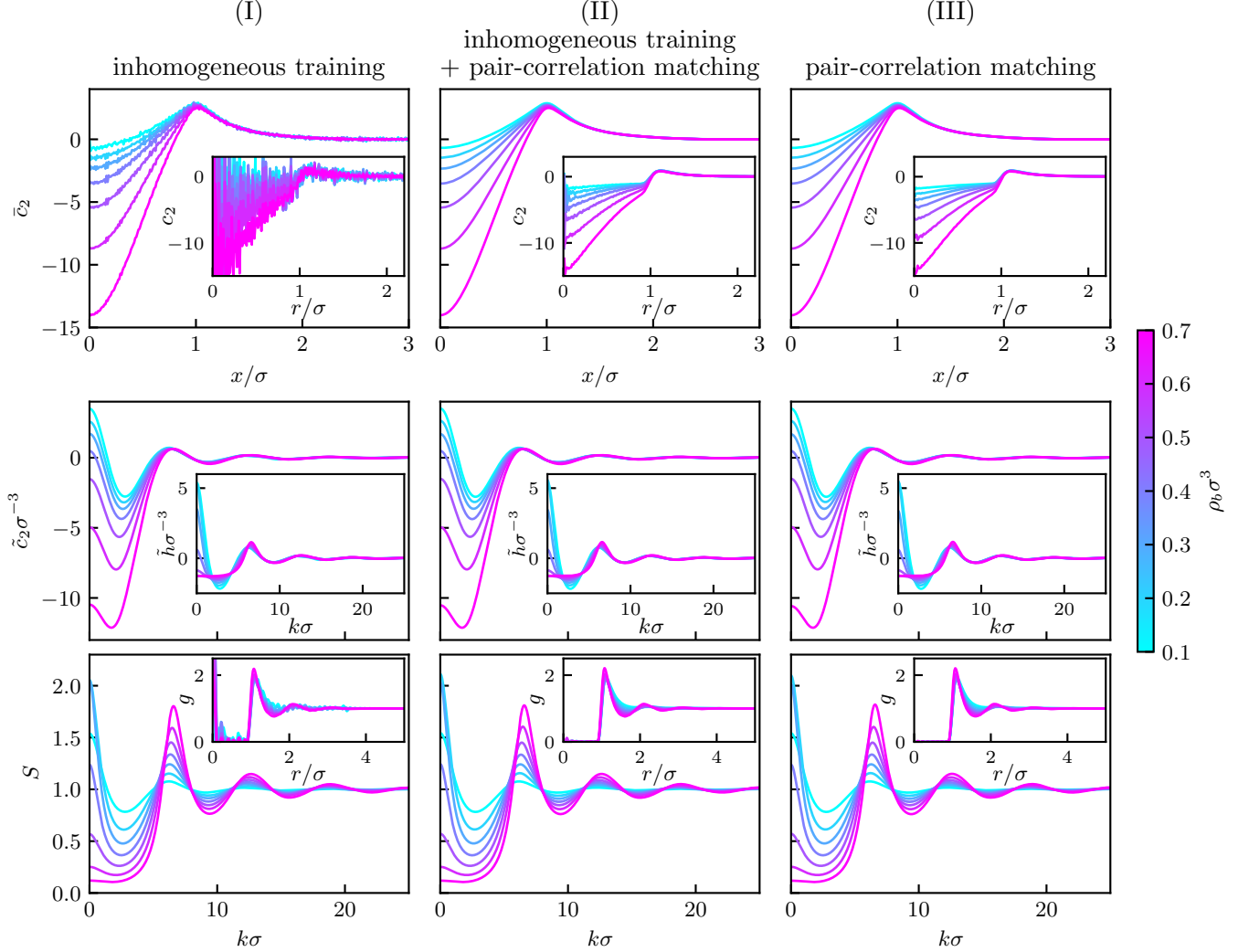


FIG. S1. Comparison of predictions of neural functionals for the truncated Lennard-Jones fluid at temperature $k_B T/\epsilon = 1.5$ and bulk densities $\rho_b \sigma^3 = 0.1, 0.2, 0.3, 0.4, 0.5, 0.6, 0.7$. Results are shown for training with purely inhomogeneous reference data (I, left column), with additional pair-correlation regularization (II, middle column) as well as with pure pair-correlation matching (III, right column). We depict the planar two-body direct correlation function $\bar{c}_2(x; \rho_b)$ and its radial representation $c_2(r; \rho_b)$ (first row), the direct and total correlation functions $\bar{c}_2(k; \rho_b)$ and $\bar{h}(k; \rho_b)$ in Fourier space (second row), as well as the static structure factor $S(k; \rho_b)$ and the radial distribution function $g(r; \rho_b)$ (third row).

A. Planar and radial geometry

The planar projection of a generic radially symmetric function $f(\mathbf{r}) = f(|\mathbf{r}|) = f(r)$ is given by

$$\bar{f}(x) = \int dy \int dz f(\sqrt{x^2 + y^2 + z^2}) = 2\pi \int_x^\infty dr r f(r), \quad (5)$$

where we indicate quantities in the reduced planar geometry by an overbar. By differentiating Eq. (5), one arrives at the inverse transformation from planar to radial geometry via

$$f(r) = -\frac{1}{2\pi r} \left. \frac{\partial \bar{f}(x)}{\partial x} \right|_{x=r}, \quad (6)$$

where we have assumed radial symmetry for $f(r)$. Applying a one-dimensional Fourier transform to the planar projection of a radially symmetric function yields directly the radially symmetric representation in Fourier space (indicated by a tilde),

$$\begin{aligned} \int dx \bar{f}(x) \exp(ik_x x) &= \int d\mathbf{r} f(r) \exp(i\mathbf{k} \cdot \mathbf{r}) \\ &= \tilde{f}(|\mathbf{k}|) = \tilde{f}(k), \end{aligned} \quad (7)$$

where $\int d\mathbf{r}$ denotes a volume integral over the entire domain.

Transforming a radially symmetric function $f(r)$ in real space to its radially symmetric Fourier representation $\tilde{f}(k)$ is facilitated by a radial Fourier(-Hankel) trans-

form,

$$\tilde{f}(k) = \frac{4\pi}{k} \int_0^\infty dr r f(r) \sin(kr). \quad (8)$$

The inverse transform of Eq. (8) is identical up to a prefactor,

$$f(r) = \frac{1}{2\pi^2 r} \int_0^\infty dk k \tilde{f}(k) \sin(kr). \quad (9)$$

The numerical evaluation of Eqs. (8) and (9) can be facilitated either via a fast Fourier transform (FFT) or via a discrete sine transform (DST). In both cases, particular care must be taken to account correctly for the discretization and the implied periodicity of the radially symmetric function to be transformed.

B. Direct and total correlation functions

For the considered two-body direct correlation function $\bar{c}_2(x; \rho_b)$, as obtained from the neural functional by autodifferentiation (4) and network evaluation in bulk with constant density input $\rho(x) = \rho_b$, Eq. (6) gives access to the more common radial representation $c_2(r; \rho_b)$, as shown in Figs. 1 and S1. Due to the required numerical differentiation and the division by r in Eq. (6), the results for $c_2(r; \rho_b)$ are prone to numerical artifacts in particular for small values of r .

Commencing with a neural functional prediction for $\bar{c}_2(x; \rho_b)$, a one-dimensional Fourier transform yields the one-body direct correlation function $\bar{c}_2(k; \rho_b)$ in radial geometry according to Eq. (7). The total correlation function $\tilde{h}(k; \rho_b)$ can then be calculated algebraically in Fourier space via the Ornstein-Zernike equation

$$\tilde{h}(k; \rho_b) = \frac{\bar{c}_2(k; \rho_b)}{1 - \rho_b \bar{c}_2(k; \rho_b)}. \quad (10)$$

From $\tilde{h}(k; \rho_b)$, one obtains the static structure factor

$$S(k; \rho_b) = 1 + \rho_b \tilde{h}(k; \rho_b), \quad (11)$$

and the transformation (9) back to direct space gives access to the radial distribution function

$$g(r; \rho_b) = h(r; \rho_b) + 1. \quad (12)$$

Neural functional predictions of the quantities in Eqs. (10)–(12) are shown in Fig. S1 at different bulk densities $\rho_b \sigma^3 = 0.1, 0.2, 0.3, 0.4, 0.5, 0.6$, and 0.7 .

III. PAIR-CORRELATION MATCHING AND REGULARIZATION

A. Preparation of simulation data

We have performed 500 simulations of the Lennard-Jones fluid in a cubic box of size $(20\sigma)^3$ at different

chemical potentials chosen uniformly in the range $-7 < \mu/\epsilon < 0$. This yields accurately sampled radial distribution functions $g(r; \rho_b)$ in $0 \leq r/\sigma \leq 10$ for bulk densities $0.01 \lesssim \rho_b \sigma^3 \lesssim 0.72$. Accessing larger bulk densities is hindered by the fact that $g(r)$ still displays non-negligible oscillations for $\rho_b/\sigma^3 \gtrsim 0.72$ for the maximal radial distance $r = 10\sigma$ in the considered simulation box. This stands in contrast to the sampling of inhomogeneous density profiles, where much larger local density maxima pose no substantial difficulty, see Sec. IA.

From the simulation data for $g(r; \rho_b)$, we calculate:

- $h(r; \rho_b)$ via the definition (12) of the total pair-correlation function,
- $\tilde{h}(k; \rho_b)$ via the radial Fourier transform (8),
- $\bar{c}_2(k; \rho_b)$ via the Ornstein-Zernike equation (10),
- $c_2(r; \rho_b)$ via the inverse radial Fourier transform (9),
- $\bar{c}_2(x; \rho_b)$ via the planar projection (5).

The planar bulk two-body direct correlation function $\bar{c}_2(x; \rho_b)$ can be compared directly to the functional derivative (4) of the one-body direct correlation functional in planar geometry,

$$\bar{c}_2(x; \rho_b) = \left. \frac{\delta c_1(0; [\rho])}{\delta \rho(x)} \right|_{\rho=\rho_b}. \quad (13)$$

Automatic differentiation is used to evaluate the functional derivative of the neural-network-based representation of $c_1(x; [\rho])$ in Eq. (13).

B. Loss functions and training procedure

Pair-correlation matching is implemented via the loss

$$L_{\text{pc}} = \sum_{i,j} \left(\bar{c}_2(x_i; \rho_{b,j}) - \bar{c}_2^{\text{ref}}(x_i; \rho_{b,j}) \right)^2 + \sum_j \left(\mu_{\text{exc}}(\rho_{b,j}) - \mu_{\text{exc}}^{\text{ref}}(\rho_{b,j}) \right)^2, \quad (14)$$

where $\bar{c}_2(x_i; \rho_{b,j})$ is calculated for the given bulk density input $\rho_{b,j}$ of bulk simulation j according to Eq. (13). The result is compared directly to the pre-calculated simulation reference $\bar{c}_2^{\text{ref}}(x_i; \rho_{b,j})$, see Sec. III A, for each discretized spatial coordinate x_i . To fix the remaining integration constant, the excess chemical potential $\mu_{\text{exc}}(\rho_b) = -k_B T c_1(x; \rho_b)$ of the neural network prediction is compared to the simulation reference $\mu_{\text{exc}}^{\text{ref}}$, which serves as an additive contribution to L_{pc} .

In general, we consider a linear combination of both loss functions,

$$L = \alpha_{\text{inhom}} L_{\text{inhom}} + \alpha_{\text{pc}} L_{\text{pc}}, \quad (15)$$

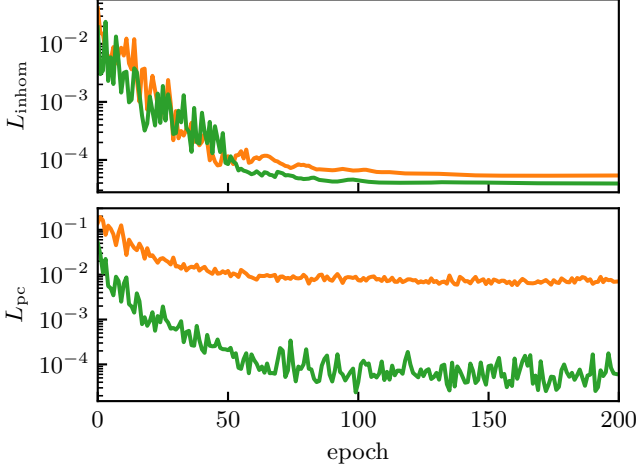


FIG. S2. Training dynamics with pair-correlation regularization (II, green) results in lower loss values L_{inhom} and L_{pc} as compared to pure inhomogeneous one-body learning without regularization (I, orange). We show the L_{inhom} and L_{pc} as a function of the training epoch.

which is used for the backpropagation and for the adaptation of the trainable parameters of the neural network. The constant factors α_{inhom} and α_{pc} control the relative influence of inhomogeneous one-body matching (2) and pair-correlation matching (14) by weighting the respective loss terms. Three choices are considered:

- (I) $\alpha_{\text{inhom}} = 1, \alpha_{\text{pc}} = 0$:
purely inhomogeneous one-body learning as in Ref. [1],
- (II) $\alpha_{\text{inhom}} = 1, \alpha_{\text{pc}} = 0.01$:
inhomogeneous one-body learning with pair-correlation regularization as introduced in this work,
- (III) $\alpha_{\text{inhom}} = 0, \alpha_{\text{pc}} = 1$:
pure pair-correlation matching inspired by Ref. [5].

C. Training dynamics and bulk results

Fig. S2 shows a comparison of the training dynamics for the individual loss terms L_{inhom} and L_{pc} for inhomogeneous one-body learning with (II) and without (I) pair-correlation regularization. The magnitude of both loss terms is decreased for the case of added pair-correlation regularization.

In Fig. S1, we depict results for bulk pair-correlation functions for each training strategy (I)–(III). Purely inhomogeneous one-body training (I) yields slightly noisy derivatives $\bar{c}_2(x; \rho_b)$, which hamper the performance of challenging numerical transformations, e.g. to obtain the two-body direct correlation function $c_2(r; \rho_b)$ in radial geometry or the radial distribution function $g(r)$. This problem is resolved both with the added pair-correlation

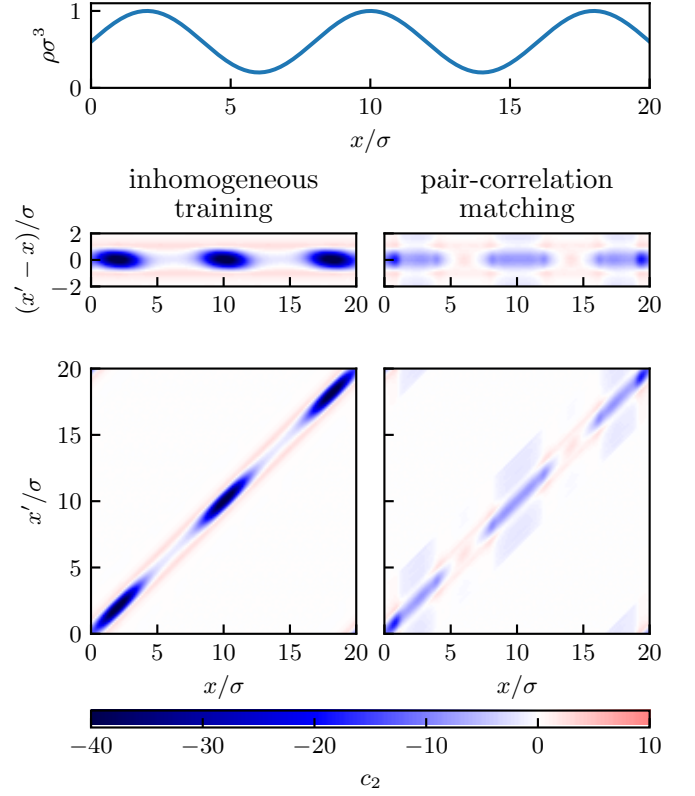


FIG. S3. Two-body direct correlation functional $c_2(x, x'; [\rho])$ for an exemplary inhomogeneous density profile $\rho(x)$ as input. We show results for neural functionals that have been trained via inhomogeneous one-body learning (I) and with pure pair-correlation matching (III). The results of the pair-correlation-matched neural functional violate the expected exchange symmetry $c_2(x, x'; [\rho]) = c_2(x', x; [\rho])$.

regularization (II) as well as with pure pair-correlation matching (III). Although the latter strategy enables accurate bulk predictions due to the supply of bulk data during training, it provides no reasonable extrapolation to inhomogeneous scenarios, as seen e.g. in faulty predictions of density profiles (Fig. 1) and of inhomogeneous two-body correlations (Fig. S3).

IV. INHOMOGENEOUS TWO-BODY CORRELATIONS AND NOETHER SUM RULES

Autodifferentiation also gives access to $c_2(x, x'; [\rho])$ for inhomogeneous density input according to Eq. (4), which enables further quality assessments of the neural functionals. As the two-body direct correlation functional formally arises as a second-order functional derivative of the excess free energy functional $F_{\text{exc}}[\rho]$, testing the expected exchange symmetry $c_2(x, x'; [\rho]) = c_2(x', x; [\rho])$ serves as a first consistency check. Additionally, testing

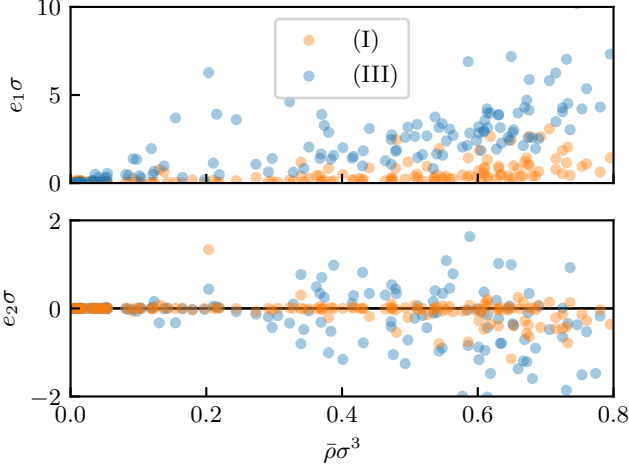


FIG. S4. Test of the Noether sum rules (16) and (17) as obtained from neural functionals trained on the basis of inhomogeneous one-body profiles (I, orange) and via bulk pair-correlation matching (III, blue). The respective errors e_1 and e_2 of the predictions are considerably larger in the latter case.

the validity of the sum rules

$$\nabla c_1(\mathbf{r}; [\rho]) = \int d\mathbf{r}' c_2(\mathbf{r}, \mathbf{r}'; [\rho]) \nabla' \rho(\mathbf{r}'), \quad (16)$$

$$\int d\mathbf{r} \rho(\mathbf{r}) \int d\mathbf{r}' \rho(\mathbf{r}') \nabla c_2(\mathbf{r}, \mathbf{r}'; [\rho]) = 0, \quad (17)$$

which result from thermal Noether invariance [6], constitutes a further valuable test of the fitness of a neural functional [1].

We depict in Fig. S3 results for $c_2(x, x'; [\rho])$ with inhomogeneous density input as obtained from neural functionals that have been trained solely with inhomogeneous one-body data (I) and with bulk pair-correlations (III), respectively. The results from the pair-correlation-matched neural functional do not display the expected symmetry of the two-body direct correlation functional upon exchanging the spatial coordinates. We recall that within the local learning strategy, the exchange symmetry is not automatically enforced, unlike in Ref. [5] where the global excess free energy acts as the output of their neural network.

In Fig. S4, we show the discrepancy of the Noether sum rules (16) and (17) as defined via $e_1 = \|\partial_x c_1(x; [\rho]) - \int dx' c_2(x, x'; [\rho]) \partial_{x'} \rho(x')\|_\infty$ and $e_2 = \int dx \rho(x) \int dx' \rho(x') \partial_x c_2(x, x'; [\rho])$. The results of the neural functional from pure pair-correlation matching (III) show considerable deviations from these sum rules.

V. NEURAL FREE ENERGY METHODS

As an alternative to working with one-body direct correlations, we also consider neural networks that give immediate access to the excess free energy functional

$F_{\text{exc}}[\rho]$. We base the construction of these neural free energy functionals on the parametrization

$$F_{\text{exc}}[\rho] = \int d\mathbf{r} \rho(\mathbf{r}) f_{\text{exc}}(\mathbf{r}; [\rho]), \quad (18)$$

which provides a well-defined localization of the excess free energy via the uniquely determined quantity

$$f_{\text{exc}}(\mathbf{r}; [\rho]) = -k_B T \int_0^1 da c_1(\mathbf{r}; [a\rho]). \quad (19)$$

A. Local learning of $f_{\text{exc}}(\mathbf{r}; [\rho])$

As a first approach, it is hence natural to construct a local neural-network-based representation of $f_{\text{exc}}(\mathbf{r}; [\rho])$. We specialize to the considered planar geometry and reuse the MLP architecture of the neural correlation functional as described in Sec. IB and shown in Fig. S5.

Training is facilitated by inhomogeneous one-body matching (2), where one determines

$$c_1(\mathbf{r}; [\rho]) = -\beta f_{\text{exc}}(\mathbf{r}; [\rho]) - \int d\mathbf{r}' \rho(\mathbf{r}') \frac{\delta \beta f_{\text{exc}}(\mathbf{r}; [\rho])}{\delta \rho(\mathbf{r}')}, \quad (20)$$

with the functional derivative of $f_{\text{exc}}(\mathbf{r}; [\rho])$ being obtained by automatic differentiation within the training loop. To be able to evaluate the integral in a local learning scheme, the arguments \mathbf{r} and \mathbf{r}' have been swapped according to the expected symmetry $\delta f_{\text{exc}}(\mathbf{r}; [\rho]) / \delta \rho(\mathbf{r}') = \delta f_{\text{exc}}(\mathbf{r}'; [\rho]) / \delta \rho(\mathbf{r})$ that arises from Eq. (19) and $c_2(\mathbf{r}, \mathbf{r}'; [\rho]) = c_2(\mathbf{r}', \mathbf{r}; [\rho])$. Crucially, this symmetry is not enforced intrinsically for an untrained neural functional for $f_{\text{exc}}(\mathbf{r}; [\rho])$, but it rather arises only after sufficient training. Utilizing the interchangeability of \mathbf{r} and \mathbf{r}' in Eq. (20) for the calculation of one-body direct correlations during training is nevertheless valid, as this leaves the true minimum of the matching condition (2) unchanged.

Applying the local neural functional for the prediction of free energy values is straightforward via the numerical evaluation of Eq. (18) for the considered density profile $\rho(x)$. For the prediction of equilibrium density profiles, $c_1(x; [\rho])$ is obtained in the considered planar geometry from Eq. (20) for use in the self-consistent solution of Eq. (3).

B. Convolutional neural network for $F_{\text{exc}}[\rho]$

As an alternative to the local learning of $f_{\text{exc}}(\mathbf{r}; [\rho])$, we use a convolutional neural network (CNN) to represent the global quantity $F_{\text{exc}}[\rho]$ while retaining the specific structure of Eq. (18). This approach bears similarity to the neural network construction in Ref. [5], but crucially differs in the utilization of a specific parametrization, Eq. (18), and in the chosen architecture, which is described in the following and illustrated in Fig. S6.

The CNN consists of 8 convolutional layers with kernel size 11, [16, 16, 32, 32, 64, 64, 16, 1] filters and dilation rates of [1, 2, 4, 8, 16, 32, 64, 1]. The hyperparameters are chosen to enable the propagation of non-local density information in a range that is similar to the window widths of the MLPs used in the previous local learning methods. We use cyclic padding for the convolutions, as is appropriate for the periodic boundary conditions of the considered systems, and employ no pooling or other coarse-graining layers, thus keeping full spatial resolution throughout the network. As a consequence of this fully convolutional architecture, the network remains applicable to virtually arbitrary system sizes and hence facili-

tates predictions “beyond-the-box” [1], as is also the case for the local learning approaches.

To arrive at the value of $F_{\text{exc}}[\rho]$ in the spirit of Eq. (18), the last layer is multiplied pointwise with the input density profile $\rho(\mathbf{r})$ and integrated over the whole domain. In particular, this implies that this last convolutional layer acts as a representation of the one-body profile $f_{\text{exc}}(\mathbf{r}; [\rho])$.

For application in the self-consistent calculation of density profiles, automatic differentiation of the $F_{\text{exc}}[\rho]$ -CNN with respect to the input density $\rho(\mathbf{r})$ yields the complete one-body direct correlation profile $c_1(\mathbf{r}; [\rho])$ to be used in Eq. (3).

-
- [1] F. Sammüller, S. Hermann, D. de las Heras, and M. Schmidt, Neural functional theory for inhomogeneous fluids: Fundamentals and applications, *Proc. Natl. Acad. Sci.* **120**, e2312484120 (2023).
 - [2] N. B. Wilding, Critical-point and coexistence-curve properties of the Lennard-Jones fluid: A finite-size scaling study, *Phys. Rev. E* **52**, 602 (1995).
 - [3] F. Sammüller, S. Hermann, D. de las Heras, and M. Schmidt, Simulation data and models for “Neural functional theory for inhomogeneous fluids: Fundamentals and applications”, 10.5281/zenodo.8380004 (2023), deposited in Zenodo.
 - [4] F. Sammüller, Simulation data and models for “Neural density functionals: Local learning and pair-correlation matching”, <https://github.com/sfalmo/local-pair-matching> (2024).
 - [5] J. Dijkman, M. Dijkstra, R. van Roij, M. Welling, J.-W. van de Meent, and B. Ensing, Learning neural free-energy functionals with pair-correlation matching, *arXiv:2403.15007 [cond-mat.soft]* (2024).
 - [6] S. Hermann and M. Schmidt, Noether’s theorem in statistical mechanics, *Commun. Phys.* **4**, 176 (2021).

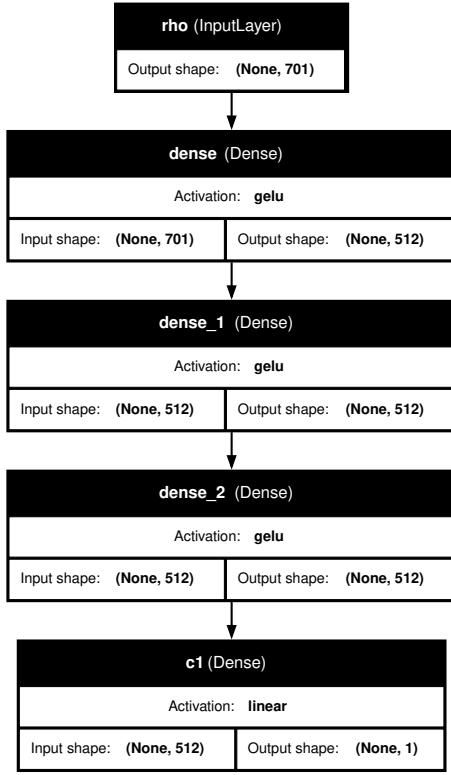


FIG. S5. Architecture of the MLP for local learning of $c_1(x; [\rho])$, cf. Sec. IB, and $f_{\text{exc}}(x; [\rho])$, cf. Sec. V A. The input and output shapes indicate the variable batch size (“None”) and the number of nodes for each layer.

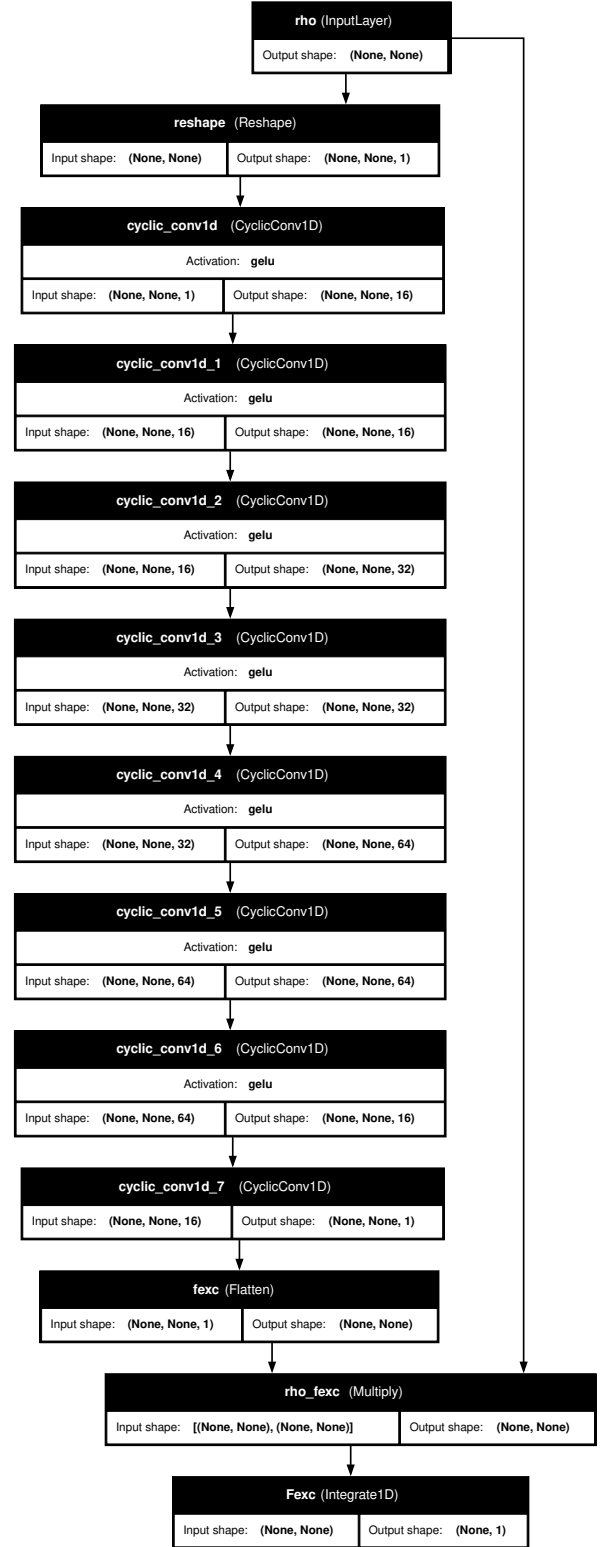


FIG. S6. Architecture of the CNN for $F_{\text{exc}}[\rho]$, cf. Sec. V B. The input and output shapes indicate the batch size, the number of spatial bins (“None” for variable size) and the number of channels.